Examination of propeller sound production using large eddy simulation

Jacob Keller, Praveen Kumar, and Krishnan Mahesh*
Department of Aerospace Engineering and Mechanics, University of Minnesota, Minneapolis, Minnesota 55455, USA

(Received 26 June 2017; published 6 June 2018)

The flow field of a five-bladed marine propeller operating at design condition, obtained using large eddy simulation, is used to calculate the resulting far-field sound. The results of three acoustic formulations are compared, and the effects of the underlying assumptions are quantified. The integral form of the Ffowcs-Williams and Hawkings (FW-H) equation is solved on the propeller surface, which is discretized into a collection of N radial strips. Further assumptions are made to reduce FW-H to a Curle acoustic analogy and a point-force dipole model. Results show that although the individual blades are strongly tonal in the rotor plane, the propeller is acoustically compact at low frequency and the tonal sound interferes destructively in the far field. The propeller is found to be acoustically compact for frequencies up to 100 times the rotation rate. The overall far-field acoustic signature is broadband. Locations of maximum sound of the propeller occur along the axis of rotation both up and downstream. The propeller hub is found to be a source of significant sound to observers in the rotor plane, due to flow separation and interaction with the blade-root wakes. The majority of the propeller sound is generated by localized unsteadiness at the blade tip, which is caused by shedding of the tip vortex. Tonal blade sound is found to be caused by the periodic motion of the loaded blades. Turbulence created in the blade boundary layer is convected past the blade trailing edge leading to generation of broadband noise along the blade. Acoustic energy is distributed among higher frequencies as local Reynolds number increases radially along the blades. Sound source correlation and spectra are examined in the context of noise modeling.

DOI: 10.1103/PhysRevFluids.3.064601

I. INTRODUCTION

Rotors are extensively used in both aerodynamic and hydrodynamic applications, e.g., propellers (airplanes, ships, submarines), helicopter rotors, wind turbines, and fans. They are a large source of unwanted noise. The production of sound by low speed rotors has received less attention in the literature than sound produced by their high-speed counterparts. Differences in speed and environment can be described by Mach number (M), which is the ratio of speed, usually total tip speed (U_{tip}), to the speed of sound (c) as $M = \frac{U_{\text{tip}}}{c}$. The focus of the present study is the sound produced by a marine (low Mach) propeller operating at design condition.

There are three main physical mechanisms of producing marine sound: (i) cavitation, (ii) vibration and deformation of the surface, and (iii) interaction of the flow with the physical surface [1,2]. The blades of a noncavitating propeller interact with the mean inflow, turbulence, and stationary velocity defects created upstream, resulting in very complex and unsteady flow conditions. At low Mach numbers, it can be shown that unsteadiness in the wake is an inefficient source of radiated sound, thus the propeller surface acts as the primary sound source.

*kmahesh@umn.edu

Surface noise is traditionally classified as either ingestion noise or self noise. Ingestion noise is due to the convection of unsteadiness present in the flow into the vicinity of the surface and is generally an inviscid mechanism. Self noise is created by viscous interaction of the surface with the flow, which can lead to vortex shedding, turbulent boundary layers, and flow separation. The surface noise can also be classified as broadband or tonal. Tonal sound results from the (i) periodic motion of blades under a steady load and (ii) periodic loading. Periodic loading can be caused by the ingestion of stationary velocity defects generated upstream or by the interaction between blades. Broadband sound is generated by the ingestion of small-scale turbulence and also by the creation and convection of turbulence in the boundary layer past the blade trailing edge.

The study of aeroacoustics dates back to Gutin [3]. Most practical analyses are built upon the work of Lighthill [4] in the 1950s. The Ffowcs-Williams and Hawkings (FW-H) equation [5] is the most general form of Lighthill's acoustic analogy, which decouples the mechanisms of sound generation from its propagation through the fluid to an observer. Historically, it has been very difficult to obtain the detailed aerodynamic knowledge required for precise numerical solution of the FW-H equation. Early work was analytical and empirical, making approximations to the geometry, the nature of sources, and the motion of the body to draw conclusions about the physics while maintaining a level of practicality and applicability. These practical assumptions of Refs. [6–8] have been used for analytical solution, shown by Refs. [9–11] for helicopters. The geometry is typically assumed to be thin or flat and of constant chord. The relative importance of impingement noise, tonal shedding noise, and trailing edge scattering noise should be also known *a priori*. Then empirical models, such as those found in the work of Graham [12], can be used to express both the spectral properties and spatial correlation of the sources [13].

More recently, work has been done to validate approximations in Amiet's model [14], account for the effects of thickness, camber, finite chord, and trailing edge back-scattering [15,16], varying chord length [17], inhomogeneity and blade-blade cascade effects [18–20], and to improve the necessary models for correlation length and source energy spectra [21–23]. Computations are able to obtain high resolution results with limited intrusion and are positioned to provide guidance on development of these models, specifically in areas where experiments are limited, such as the vicinity of the trailing edge.

Reynolds-averaged Navier-Stokes (RANS) and unsteady RANS (URANS) approaches are popular for computing far-field sound among the fan and turbine communities due to their reduced computational cost. Brentner and Farassat [24] and Tadamasa and Zangeneh [25], note that RANS and URANS are unable to accurately capture the broadband turbulent noise. Wall-resolved large eddy simulation (LES) is able to provide the spatially and temporally accurate flowfield, including turbulence. Thus, the unsteady propeller loading from the LES may be supplied as input to the numerical solution of the FW-H equation to reduce the number of assumptions necessary to obtain far-field sound.

Arakawa *et al.* [26] were the first to use compressible LES in combination with FW-H for a two bladed wind turbine at low Mach number. However, due to limited computational resources, only a fraction of a rotation was simulated and results were only presented for the near field. More recently, Wang *et al.* [27–29] have used incompressible LES to investigate noise produced by a low Mach fan due to ingestion of both homogeneous, isotropic turbulence and the wake of a turbulent cylinder. The interaction between the acoustic waves and the flowfield becomes very weak with decreasing Mach number; their effect on the flowfield and sound sources may be neglected, and incompressible LES may be used.

The present results are obtained from LES, which reduces the computational cost compared to a full direct simulation. Kumar and Mahesh [30] and Keller *et al.* [31] used incompressible LES to analyze the physics of the flow field generated by the five-bladed propeller, DTMB 4381, at design operating condition showing good agreement with experiments. In this paper, the LES solution is used to predict the far-field sound for a FW-H strip acoustic analogy, Curle strip acoustic analogy (CSA), and a point-force dipole model (PFD). Each of these formulations can be derived from the full FW-H equation with varying levels of generality; the comparative accuracy of the far-field sound

is assessed quantitatively with respect to the underlying assumptions. The CSA as well as the FW-H analogies are derived for the physical surface of the propeller. Each blade is discretized into a number of radial strips and the effects of this blade resolution on the acoustics (i.e., acoustic compactness) are examined. Two discretizations of five and ten strips per blade are used.

The objective of the present work is to (i) calculate the sound produced by the propeller at design operating condition, (ii) assess the performance of various acoustic formulations, (iii) analyze the mechanisms of sound production, and (iv) provide empirical guidance for noise modeling. The simulation details and acoustic formulations are described in Secs. II and III, respectively. Results are used to assess the three acoustic formulations and discuss the physics of sound generation, by the propeller as a whole (Sec. IV) and by the hub (Sec. V) and by blades (Sec. VI) independently. The implications of the results for noise modeling is discussed in Sec. VII. Finally, a brief summary of the paper is presented in Sec. VIII.

II. PROPELLER SIMULATION DETAILS

Accurate prediction of the sound generated by a propeller relies on the accuracy of the unsteady blade loading obtained from numerical simulation. Capturing the complicated unsteady physical mechanisms of sound generation in the flow field is vital to the sound calculation. Segalini and Inghels [32] examined confinement effects on measurements of wind-turbines and propellers, showing that the domain size affects the width and pitch of the propeller wake, hence, the size of the domain should be large enough to avoid any confinement effects. The computation of acoustic signals is dependent on the frequencies to be resolved and, as such, requires high-fidelity knowledge of the flow field both spatially and temporally. Both of these requirements make this problem prohibitively expensive for direct numerical simulation (DNS); LES is able simulate a large domain extent at the necessary temporal resolution. The accuracy and capability of LES to predict complex phenomena are demonstrated by Mahesh *et al.* [33].

A. Numerical method

In LES, large-scale flow features are resolved by the spatially filtered Navier-Stokes equations, whereas the effect of the small scales is modeled. The present simulations are performed in a frame of reference that rotates with the propeller; the spatially filtered incompressible Navier-Stokes equations, in the rotating frame of reference, are formulated for the absolute velocity vector as follows:

$$\frac{\partial \overline{u}_i}{\partial t} + \frac{\partial}{\partial x_j}[\overline{u}_i(\overline{u}_j - \epsilon_{jkl}\Omega_k x_l)] = -\frac{\partial \overline{p}}{\partial x_i} - \epsilon_{ijk}\Omega_j \overline{u}_k + \nu \frac{\partial^2 \overline{u}_i}{\partial x_j x_j} - \frac{\partial \tau_{ij}}{\partial x_j},$$
$$\frac{\partial \overline{u}_i}{\partial x_i} = 0, \tag{1}$$

where x_i are the coordinates of the rotating, noninertial reference frame, u_i is the velocity measured in the nonrotating frame, p is the pressure, Ω_j is the angular velocity of the rotating frame, ν is the kinematic viscosity, ϵ_{ijk} denotes the permutation tensor, and the approximation $\overline{u_i \epsilon_{jkl}\Omega_k x_l} \approx \overline{u}_i \epsilon_{jkl}\Omega_k x_l$ is used. The terms containing Ω_j in Eq. (1) take into account the effect of the rotating reference frame which is noninertial; the Coriolis acceleration is represented by $\frac{\partial}{\partial x_j}(-\overline{u}_i \epsilon_{jkl}\Omega_k x_l)$, whereas $-\epsilon_{ijk}\Omega_j \overline{u}_k$ is the centrifugal acceleration. The overbar $\overline{(\,)}$ denotes the spatial filter and $\tau_{ij} = \overline{u_i u_j} - \overline{u}_i \overline{u}_j$ is the subgrid stress. The subgrid stress is modeled by the dynamic Smagorinsky model [34,35]. The Lagrangian time scale is dynamically computed based on surrogate-correlation [36] of the Germano-identity error [37].

Equation (1) is solved using the algorithm developed by Mahesh *et al.* [38] for unstructured grids. The algorithm is derived to be robust without use of numerical dissipation by discretely conserving kinetic energy. Discrete energy conservation ensures that the flux of kinetic energy has contributions only from the boundary faces. It is a finite volume method where the Cartesian

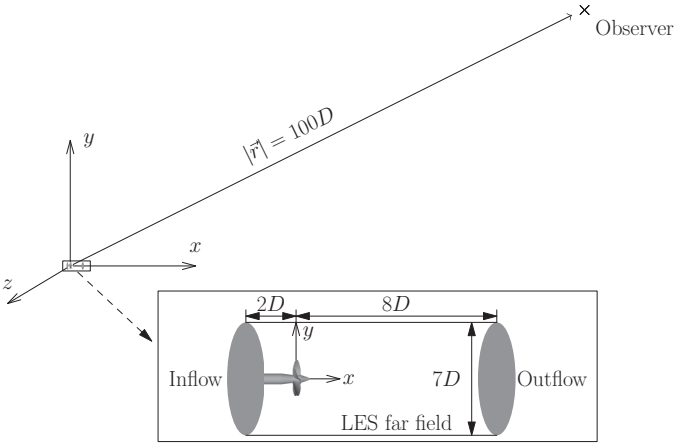

FIG. 1. The setup of the acoustic problem, computational domain, and boundary conditions. The propeller rotates about the x axis with the origin located at the center of the rotor disk. All acoustic results were calculated at an observer radius of $100D$ at 360 locations in the xy plane; one such observer location is shown.

velocities and pressure are stored at the centroids of the cells; the face normal velocities are stored independently at the centroids of the faces. A predictor-corrector approach is used; the predicted velocities at the control volume centroids are first obtained and then interpolated to obtain the face normal velocities. The predicted face normal velocity is projected so that the continuity equation, shown in Eq. (1), is discretely satisfied, yielding a Poisson equation for pressure, which is solved iteratively using a multigrid approach. The pressure field is used to update the Cartesian control volume velocities using a least-square formulation. Time advancement is performed using an implicit Crank-Nicolson scheme. The algorithm has been used extensively in previous studies of this propeller in multiple configurations and operating conditions [30,39–46] as well as other problems over a range of Reynolds numbers [38].

B. Computational setup

The simulations are performed on propeller DTMB 4381 at design conditions, i.e., an advance ratio ($J = U/nD$) of 0.889 and a Reynolds number ($\mathrm{Re} = UD/\nu$) of 894 000. U is the free-stream velocity, n is the propeller rotational speed, and D is the diameter of the propeller disk. The propeller geometry, computational domain, and boundary conditions used in the present work are identical to those used in the work of Kumar and Mahesh [30]. The propeller is right handed with variable pitch, no skew, and no rake; the geometric details of the propeller are reported by Bridges [47]. The external boundary of the LES computational domain is a cylinder of diameter $7D$ and length $10D$. The reference coordinate system is chosen such that the blades of the propeller are located at the origin and the flow is in the positive x direction. The propeller is positioned $2D$ downstream of the inflow boundary, as shown in Fig. 1.

Freestream boundary conditions are prescribed both at the inflow and radial boundaries; convective boundary conditions are prescribed at the outflow. The velocities in the governing Eqs. (1) are measured in the nonrotating reference frame and the velocity boundary conditions are consistent. The velocity boundary conditions on the rotor are $\vec{\boldsymbol{u}} = \vec{\boldsymbol{\Omega}} \times \vec{\boldsymbol{r}}$ and on the shaft are no-slip conditions, $\vec{\boldsymbol{u}} = 0$.

The grid is designed carefully to capture all the essential features of the flow field and is clustered close to all solid surfaces. Ten layers of hexahedral cells are extruded from the surface with minimum wall-normal spacings of $1.7 \times 10^{-3} D$ on the blades and $1.7 \times 10^{-4} D$ on both the hub and shaft surfaces to resolve near-wall flow features. A growth ratio of 1.02 is applied at all solid surfaces to

transition from fine to coarser resolution away from the surface. The grid is refined in the near-wake region of the propeller to capture the small scales.

The entire grid consists of 181 million hexahedral control volumes and is partitioned over 2048 processors. The simulations are performed with a nondimensional time step of 0.001 unit, nondimensionalized with U and D, corresponding to 1 rotation in 10 668 computational time steps.

III. ACOUSTIC COMPUTATION

A. Acoustic formulations

The FW-H equation is derived in detail by Brentner and Farassat [24]; it has three source terms, which are typically referred to as the monopole, dipole, and quadrupole terms. The integral form of the equation is derived using the free-space Green's function, which is valid for all sources in the embedded flow problem of the FW-H equation.

The observer space and time variables, respectively, are $\vec{x}$ and t and the acoustic source space-time variables are $\vec{y}$ and τ. The condition $t = \tau + |\vec{r}|/c$ relates the source and observer, where $\vec{r} = \vec{x} - \vec{y}$ is the radiation vector from the acoustic source to the observer, and c is the speed of sound in the undisturbed fluid. The observer is assumed to be at rest. The integration is performed over a prescribed acoustic surface, which in the present work is chosen to be the physical propeller surface. The FW-H equation for a physical surface is

$$4\pi p'(\vec{x},t) = \frac{\partial}{\partial t}\int_S \left[\frac{\rho_0 v_n + \rho(\cancelto{0}{u_n} - v_n)}{|1-M_r||\vec{r}|}\right]_{\text{ret}} dS(\vec{y},\tau) - \frac{\partial}{\partial x_i}\int_S \left[\frac{\cancelto{0}{\rho u_i}(\cancelto{0}{u_n} - v_n) + f_i}{|1-M_r||\vec{r}|}\right]_{\text{ret}} dS(\vec{y},\tau) + \frac{\partial^2}{\partial x_i x_j}\int_{V_{\text{ext}}} \left[\frac{T_{ij}(\vec{y},\tau)}{|1-M_r||\vec{r}|}\right]_{\text{ret}} dV_{\text{ext}}(\vec{y},\tau), \tag{2}$$

where ρ and ρ_0 are the local and static densities of the fluid, $u_n = 0$ is the normal velocity of the fluid at the impenetrable acoustic surface, v_n is the normal velocity of the acoustic surface, and $M_r = v_r/c$ is the Mach number of the surface in the direction of $\vec{r}$. The local force on the surface is expressed in terms of the compressive stress tensor (P_{ij}) and the local normal vector (n_j) as $f_i = \Delta P_{ij} n_j$ and T_{ij} is Lighthill's stress tensor [4]. The subscript ret implies that the integrand is evaluated at the emission time (τ_e) and emission position $(\vec{r}_e)$ which implies $t = \tau_e + |\vec{r}_e|/c$ and the subscript ext implies that the volume integral is performed on the volume external to the acoustic integration surface.

When the acoustic surface corresponds to a physical (impenetrable) surface, the monopole and dipole may be referred to as the thickness and loading terms, respectively, giving some insight to their physical nature. It can be shown, from scaling arguments [4,48–50], that the acoustic efficiency of quadrupoles decreases with a decrease in Mach number, when compared to monopole and dipole sources. This eliminates the need to compute the quadrupole volume integral and greatly reduces the computational cost of the analogy.

If the acoustic surface is constrained to be immobile, i.e., there is no normal velocity of the surface, $v_n = 0$, and $M_n = 0$, then Curle's [51] acoustic analogy for a physical surface is recovered from Eq. (2):

$$4\pi p'(\vec{x},t) = -\frac{\partial}{\partial x_i}\int_S \left[\frac{f_i}{|\vec{r}|}\right]_{\text{ret}} dS(\vec{y},\tau). \tag{3}$$

The assumption neglects the displacement of fluid by the movement of the surface and will be examined in Sec. IV.

Blake [1] shows that, when the acoustic surface is acoustically compact, the i component of the net force $[F_i = \int_S f_i dS(\vec{y})]$ can be modeled at some point $\vec{y}_0$ contained by the surface $S(\vec{y})$. The propeller can be considered compact when the acoustic wavelength of the radiated sound, which is dependent on the speed of sound of the medium (c) and frequency (f) as $\lambda = c/f$, is much larger than the characteristic size (L) of the acoustic surface. Thus, when compact, the presence of the

FIG. 2. A schematic showing how the propeller is broken down into strips for the case of five strips per blade resulting in 25 strips in total. The strips are equal in thickness along the radial direction.

surface is modeled by the equivalent point force on the fluid where F_i is only a function of τ and the radiation vector is constant over the surface, $\vec{r} = \vec{x} - \vec{y_0}$. Equation (3) becomes

$$p'(\vec{x},t) = -\frac{1}{4\pi}\frac{\partial}{\partial x_i}\frac{F_i}{|\vec{r}|}\bigg|_{\text{ret}}. \tag{4}$$

The validity of this assumption will be examined in Sec. IV. For a general source $Q_i(\tau)$, it can be shown that

$$\frac{\partial Q_i}{\partial x_i} = -\frac{\hat{r}_i}{c}\frac{\partial Q_i}{\partial \tau}, \tag{5}$$

where $\hat{r}_i$ is the component of the unit radiation vector in the i direction. In the far field,

$$\frac{\partial Q_i}{\partial \tau} = \frac{\partial}{\partial \tau}\left(\frac{F_i}{|\vec{r}|}\right) = \frac{1}{|\vec{r}|}\frac{\partial F_i}{\partial \tau} - \frac{F_i}{|\vec{r}|^2}\frac{\partial |\vec{r}|}{\partial \tau} \approx \frac{1}{|\vec{r}|}\frac{\partial F_i}{\partial \tau}, \tag{6}$$

where $Q_i = F_i/|\vec{r}|$. Thus, the Curle analogy becomes

$$p'(\vec{x},t) \approx \frac{1}{4\pi}\frac{\hat{r}_i}{|\vec{r}|c}\frac{\partial F_i}{\partial \tau}\bigg|_{\text{ret}} \tag{7}$$

$$= \frac{1}{4\pi}\frac{\hat{r}_i}{|\vec{r}|c}\frac{\partial F_i(\tau_e)}{\partial t}. \tag{8}$$

If the propeller is discretized into k integration surfaces composed of radial strips, as shown in Fig. 2 where $k = 5$, the linear nature of the governing equations can be leveraged, allowing the k sources to be treated independently and superimposed. This is done for the Curle analogy by Blake [52] and the FW-H analogy by Succi [10].

The assumption that the acoustic surface is stationary in the derivation of the Curle acoustic analogy remains intact when the point forces are allowed to rotate about the origin. The compact point forces can be thought of as moving on an axisymmetric ring of radius $|\vec{y}_0|$, which includes the space between the blades. The symmetry of the ring allows the locations of the point forces to move on the immobile surface; therefore, the specific geometry of the propeller is neglected [consistent with the assumptions of Eq. (4)], but the effects of compactness and rotation can be examined.

The notation of the subscript k is adopted to denote variables that are strip dependent and does not follow the summation convention, i.e., $p'_k(\vec{x},t), \vec{F}_k$, and $\vec{r}_k$ are the pressure, net force, and radiation vector of the kth strip. The k concentric rings are then superposed to predict the acoustic field generated by the whole propeller. Thus,

$$p'(\vec{x},t) = \sum_k p'_k(\vec{x},t) = \frac{1}{4\pi}\frac{\hat{r}_{k_i}}{|\vec{r_k}|c}\frac{\partial F_{k_i}(\tau_e)}{\partial t}. \tag{9}$$

will be referred to as the Curle strip analogy (CSA). This was the result obtained by Lowson and Ollerhead [53] for a helicopter modeled as a collection of rotating point forces.

In the limit of $k = 1$, the entire propeller surface is assumed to be acoustically compact ($\lambda \gg D$) and all phase information between correlated sources across the surface is lost. The propeller is

reduced to a point at the origin ($\hat{r}_i \to \hat{x}_i$), $\frac{\partial}{\partial \tau}$ becomes $\frac{\partial}{\partial t}$, and the source strength becomes equal to the net force on the propeller. Equation (8) is recovered and will be called the point-force dipole (PFD) in the remainder of the text.

Succi [10] originally derived the FW-H equation for compact radial strips on a physical surface. The result, reproduced by Farassat and Succi [11], is the analogy employed in this study, excluding near-field terms.

$$p'_k(\vec{\boldsymbol{x}},t) = \frac{\rho_0}{4\pi}\left\{\frac{\psi_k}{\left(1-M_{k_r}\right)}\frac{\partial}{\partial\tau}\left[\frac{1}{\left(1-M_{k_r}\right)}\frac{\partial}{\partial\tau}\left(\frac{1}{|\vec{\boldsymbol{r}}_{\boldsymbol{k}}|\left(1-M_{k_r}\right)}\right)\right]\right\}_{\text{ret}} + \frac{1}{4\pi}\left\{\frac{1}{|\vec{\boldsymbol{r}}_{\boldsymbol{k}}|\left(1-M_{k_r}\right)^2}\left[\frac{\hat{r}_{k_i}}{c}\frac{\partial F_{k_i}}{\partial\tau}+\frac{F_{k_i}\hat{r}_{k_i}}{\left(1-M_{k_r}\right)}\left(\frac{\hat{r}_{k_j}}{c}\frac{\partial M_{k_j}}{\partial\tau}\right)\right]\right\}_{\text{ret}}, \tag{10}$$

where M_i is the mach number of the moving surface, $M_{k_i} = \frac{1}{c}\frac{\partial y_{0k_i}}{\partial\tau}$. As pointed out by Farassat and Succi [11], this result matches Lowson's [54] result. The first term, in square brackets, is the monopole (thickness) term and is dependent on the volume of the strip ψ_k, which is not present in the CSA. The second term is the dipole (loading) term. As $M_{k_j} \to 0$, Doppler amplification and rotational acceleration are neglected, thus the loading term reduces to the CSA.

In the case of a propeller rotating about the 1-axis at $\vec{\boldsymbol{\Omega}} = \Omega\hat{e}_1$,

$$\frac{\partial y_{0k_i}}{\partial\tau} = \begin{cases} 0 & \text{if } i=1, \\ -\Omega y_{0k}\sin(\Omega\tau) & \text{if } i=2, \\ \Omega y_{0k}\cos(\Omega\tau) & \text{if } i=3. \end{cases}$$

With the motion of the propeller prescribed analytically, the time derivatives of Eq. (10) can be evaluated,

$$\begin{aligned} p'_k(\vec{\boldsymbol{x}},t) = \frac{\rho_0\psi_k}{4\pi}\Bigg[&\frac{3}{|\vec{\boldsymbol{r}}_{\boldsymbol{k}}|\left(1-M_{k_r}\right)^5}\left(\frac{\Omega^2 y_{0k}}{c}\right)^2\left(\hat{r}_{k_2}\cos(\Omega\tau)-\hat{r}_{k_3}\sin(\Omega\tau)\right)^2 \\ &+\frac{1}{|\vec{\boldsymbol{r}}_{\boldsymbol{k}}|\left(1-M_{k_r}\right)^4}\left(\frac{\Omega^3 y_{0k}}{c}\right)\left(\hat{r}_{k_2}\sin(\Omega\tau)-\hat{r}_{k_3}\cos(\Omega\tau)\right)\Bigg]_{\text{ret}} \\ &+\frac{1}{4\pi c}\left\{\frac{1}{|\vec{\boldsymbol{r}}_{\boldsymbol{k}}|\left(1-M_{k_r}\right)^2}\left[\hat{r}_{k_i}\frac{\partial F_{k_i}}{\partial\tau}-\frac{F_{k_i}\hat{r}_{k_i}}{\left(1-M_{k_r}\right)}\left(\frac{\Omega^2 y_{0k}}{c}\right)\left(\hat{r}_{k_2}\cos(\Omega\tau)-\hat{r}_{k_3}\sin(\Omega\tau)\right)\right]\right\}_{\text{ret}}. \end{aligned} \tag{11}$$

It should be pointed out that the only assumptions about the nature of the sound sources for FW-H are (i) the low Mach number allows the exterior quadrupole sources to be neglected and (ii) the integration surfaces are acoustically compact. The assumption of acoustic compactness leads to the interference of both correlated and uncorrelated sources alike. The CSA is further restricted by the assumption of a stationary surface, which neglects the effects of thickness and also the acceleration of the forces. No assumptions have been made regarding the character of the sound sources (e.g., broadband, tonal), where they are produced on the surface (e.g., leading edge, trailing edge, along the surface), nor their correlation.

B. Application of acoustic methods

To increase computational efficiency, all vectors and forces are computed in the inertial frame attached to the origin, rather than in the rotational frame of the propeller. Equation (8) will be applied at the propeller origin with strength equal to the net force on the blades. Equation (9) will be applied at each of the rotating strip locations with the strength equal to the net force on the strip; the

TABLE I. Flow parameters and mean values of thrust and torque coefficients for DTMB 4381 and $J = 0.889$.

	Re	Re_c	$\langle K_T \rangle$	$\langle K_Q \rangle$
Kumar and Mahesh 2017 (LES)	8.9×10^5	8.3×10^5	0.21	0.041
Jessup *et al.* 2004 (OW)	11×10^5	10.2×10^5	0.201	0.0421
Jessup *et al.* 2006 (WT)	8.9×10^5	8.3×10^5	0.18	0.038
Hecker and Remmers 1971 (OW)	6.47×10^5	6×10^5	0.211	0.042

compactness of the propeller and rotation of the sources will be examined. Equation (11) is applied to more completely examine rotation by including the effects of the blade thickness and Doppler amplification due to the surface motion relative to the observer.

The effects of acoustic compactness are examined through the comparison of two surface discretizations, where five and ten strips comprise each propeller blade, for both the CSA and FW-H methods. Sound below $f = c/D \approx 1\,000$ Hz has a wavelength (λ) much larger than the diameter of the propeller (D); sound below $f \approx 10\,000$ Hz has a wavelength much larger than the characteristic size of the radial strips. The compactness of the propeller breaks down for the PFD [Eq. (8)] at high frequencies; the CSA and FW-H are valid over a much wider range for the present discretizations.

Lastly, all sound calculations are performed at an observer radius of $100D$ from the propeller origin at 360 locations in the xy plane, as shown in Fig. 1.

IV. PROPELLER SOUND

A. Propeller loading

In this section, the computed flow field and the unsteady loads of the propeller, which are used as input to the acoustic models, are discussed. For a detailed validation of the LES results and description of the mechanisms of the propeller wake evolution, the reader is referred to Kumar and Mahesh [30]. Kumar and Mahesh also demonstrated the grid convergence of both the flowfield and resulting propeller loads.

The net load on the propeller can be decomposed into thrust (axial) and side-force (rotor plane) components. Thrust (T) can be nondimensionalized using ρ, n, and D as the thrust coefficient, $K_T = \frac{T}{\rho n^2 D^4}$. Likewise, the axial component of the moment of force, torque (Q), can be nondimensionalized as $K_Q = \frac{Q}{\rho n^2 D^5}$. The computed mean K_T and K_Q are compared to the experimental results of Hecker and Remmers [55] and Jessup *et al.* [56,57] as shown in Table I. Jessup *et al.* [56,57] report experiments conducted in a 36 in. water tunnel (WT) and open-water towing tank (OW), Hecker and Remmers [55] report only experiments conducted in an open-water towing tank. LES results for $J = 0.889$ (Table I) show good agreement with experiments for the mean value of thrust and torque coefficients. The measured value of the loads is smaller in the water tunnel, possibly due to tunnel confinement effects of the tunnel and the blockage effects of the experimental apparatus. The computed values of mean thrust and torque coefficients show good agreement with tow-tank data.

Thrust comprises both viscous and pressure forces (note that the viscous force is negative); the magnitudes of the viscous contribution to thrust and the pressure contribution are compared in Fig. 3(a). The pressure force generated by the propeller is two orders of magnitude larger than the viscous force due to the high Reynolds number of the flow.

To understand the contribution to K_T from different parts of the blade, the blade is split into 10 equal parts in the radial direction, on the pressure and suction sides each. The contribution from each part is shown in Fig. 3(b). Note that most of the thrust is generated in the region around the mid-span ($\approx 0.7R$) of the blades. In that region, the blade has the largest chord-length, and hence, a larger surface area upon which lift is generated.

At design operating conditions, the side-force component of the net propeller force is very small compared to thrust. Nondimensionalizing the same as thrust, the mean value $\langle K_{F_y} \rangle$ is 3.2×10^{-8}

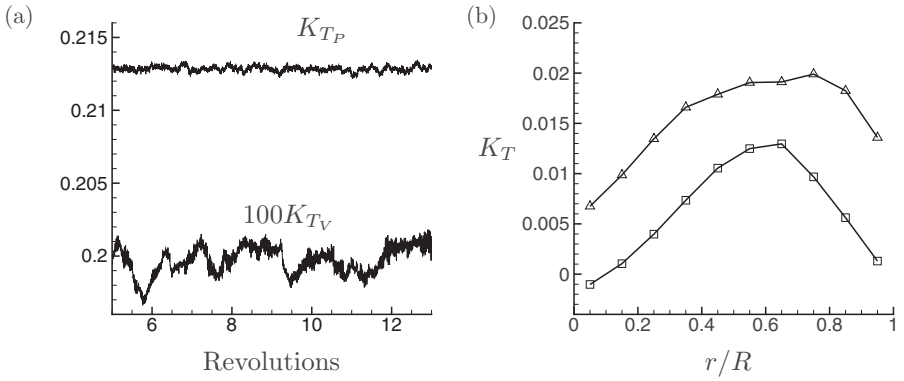

FIG. 3. (a) Pressure and viscous contribution to thrust (K_{T_P}, K_{T_V}) generated by the propeller and (b) radial distribution of thrust coefficient: pressure side, –△–; suction side, –□–.

compared to thrust, $\langle K_{F_y} \rangle = 0.21$. However, sound is intrinsically unsteady and it is important to examine the inherent amounts of unsteadiness that accompany the loads on the propeller. The root-mean square (RMS) of the time derivatives of K_T and K_{F_y}, $\dot{K}_{T_{\mathrm{RMS}}}$ and $\dot{K}_{F_{y,\mathrm{RMS}}}$, respectively, are 0.54 and 0.20. Although the magnitude of the side force is small, it is important to sound production.

B. Sound field

Figure 4 shows directivity plots of sound pressure level (SPL) in the xy plane, perpendicular to the rotor plane, for each method using ten strips. SPL is calculated as $20\log_{10}(\frac{p_{\mathrm{RMS}}}{p_{\mathrm{ref}}})$ where $p_{\mathrm{ref}} = 1\ \mu$Pa. The angle $\theta = 0^\circ$ is aligned with the direction of the propeller wake and all sound is calculated at an observer radius of $100D$. The propeller creates a sound field characteristic of a dipole source, indicated by the two lobes along the axis of rotation. A true dipole source would have perfect cancellation in the rotor plane whereas the propeller shows a decrease of only 8.63 dB in Fig. 4. While thrust unsteadiness is the main source of sound, oscillations in side-force are generating a noticable level of sound.

Note that there are two PFD directivities plotted; the dashed line represents the sound generated when the net force is calculated over the whole of the propeller (hub and blades) whereas the solid line represents the sound generated when the net force is calculated only over the surface of the blades. The hub can be thought of as being an additional strip applied at the propeller origin. Ergo, it is indifferent to the various rotation and geometry assumptions between the CSA and FW-H.

The signature of hub sound is primarily seen in the rotational plane where it accounts for up to 20% of p_{RMS}; the level of sound generated by the hub is much smaller than blade sound along the axis of rotation ($\approx 1\%\ p_{\mathrm{RMS}}$). The contribution of the hub is constant across the various methods due to the rotational symmetry of the hub. Hence, any differences between the methods are not caused by the flow on the hub, examined independently (Sec. V) from blade generated sound (Sec. VI).

Table II shows a comparison of each of the strip methods against the point-force dipole; it shows the average difference of the methods for both five and ten strips. For each of the acoustic analogies, the average difference between results computed using five strips and ten strips are below 0.04% of p_{RMS}, whereas the comparative difference between the CSA and the FW-H method is approximately 1% of p_{RMS}, and 14% when compared with the PFD. The inclusion of the thickness source and the acceleration of the surface forces accounts for the 1% difference between CSA and FW-H.

Figure 5 shows the additional thickness and loading sources of FW-H are much much smaller than the the overall sound levels of CSA. Most marine propellers have thin cross sections and slower rotational speeds than their aerial counterparts. Thus it is expected that for a rotor producing a comparable amount of thrust at a higher Mach number in air, the differences between CSA and FW-H would be more evident.

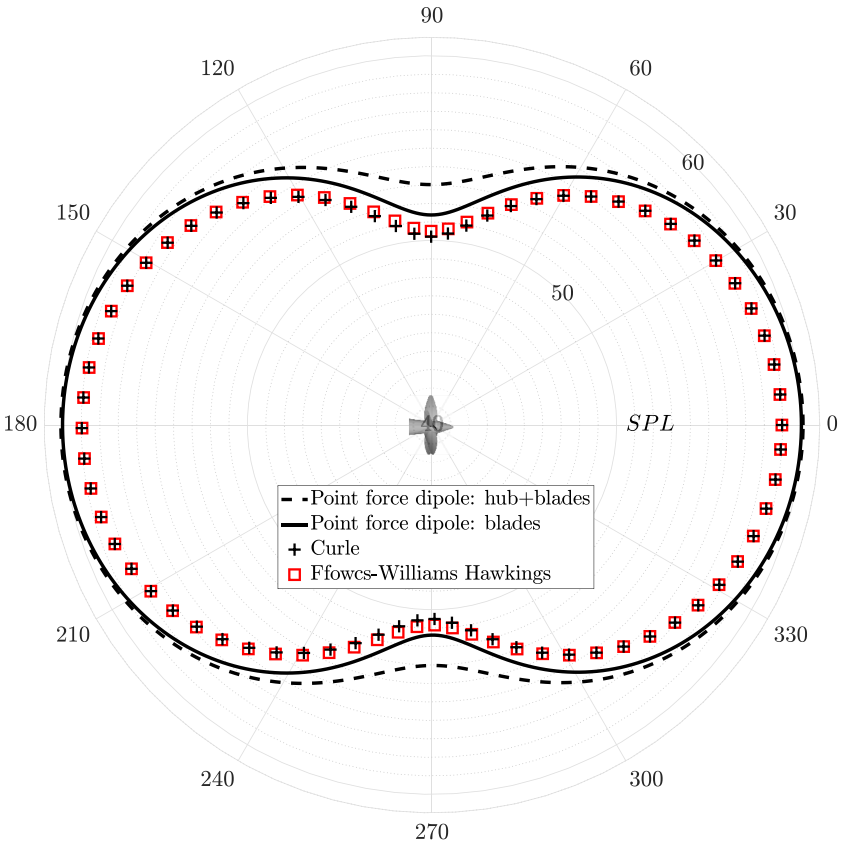

FIG. 4. Directivity of total sound pressure level (SPL) at $r = 100D$, perpendicular to the rotor plane comparing each of the models for a blade discretization of ten strips. Every fifth data point has been plotted for clarity. The origin is set to 40 dB.

Overall, there is a decrease in SPL that occurs for both the CSA and FW-H methods when compared with the PFD. Table II shows an average gain in accuracy of 14% obtained by discretizing the propeller into strips. The discretization allows the assumption of acoustic compactness to be satisfied over a wider range of frequencies, as seen in Figs. 6(b) and 6(c). Frequencies beyond the compact frequency limit of 1 kHz for the PFD, established in Sec. III B, still contain significant acoustic energy. Above 1 kHz, the wavelength of sound is comparable to the propeller diameter, but the PFD does not account for the destructive interference that occurs. For five strips per blade, the CSA and FW-H have a much greater compactness limit of 10 kHz, larger than the Nyquist frequency

TABLE II. Mean difference of root-mean-square pressure between the strip methods and the point-force dipole method for both five and ten strips.

	Average difference with PFD (%)	
Method	5 strips	10 strips
CSA	13.998	14.023
FW-H	13.090	13.094

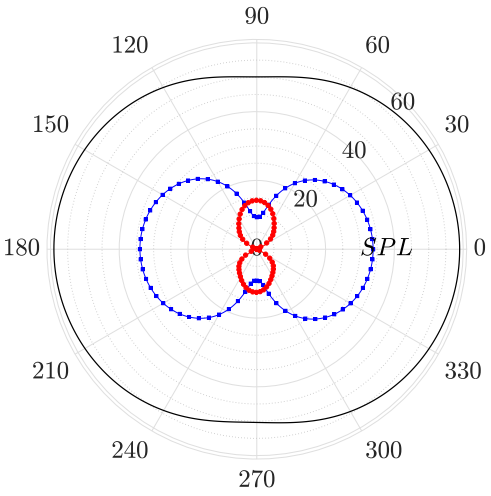

FIG. 5. Comparison of the additional FW-H loading (–■–) and thickness (–●–) sources with CSA (–). Every fifth point has been plotted for clarity. The origin is 0 dB.

of the present work which is 5 882 Hz. The effects of sampling were examined by increasing the Nyquist frequency by a factor of ten (not shown here) and the conclusions did not change.

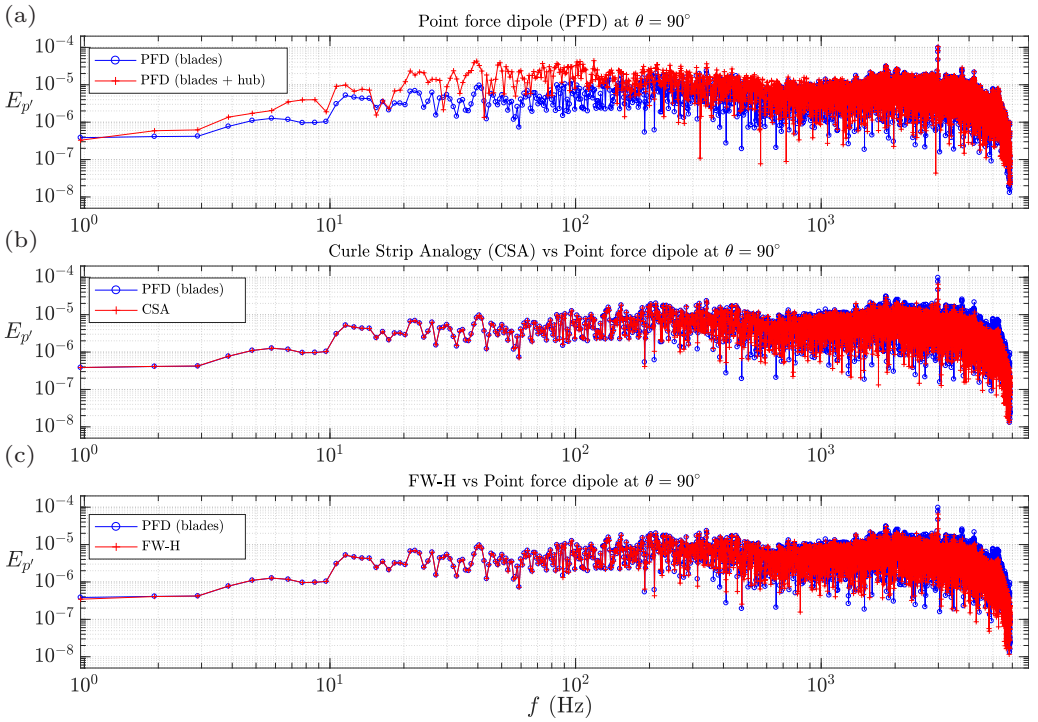

FIG. 6. Comparison of the energy spectra of the point-force dipole to: (a) the point-force dipole with the contribution of the hub, (b) the Curle strip acoustic analogy, and (c) the Ffowcs-Williams and Hawkings strip acoustic analogy. Spectra are calculated at an observer position of $\theta = 90^\circ$.

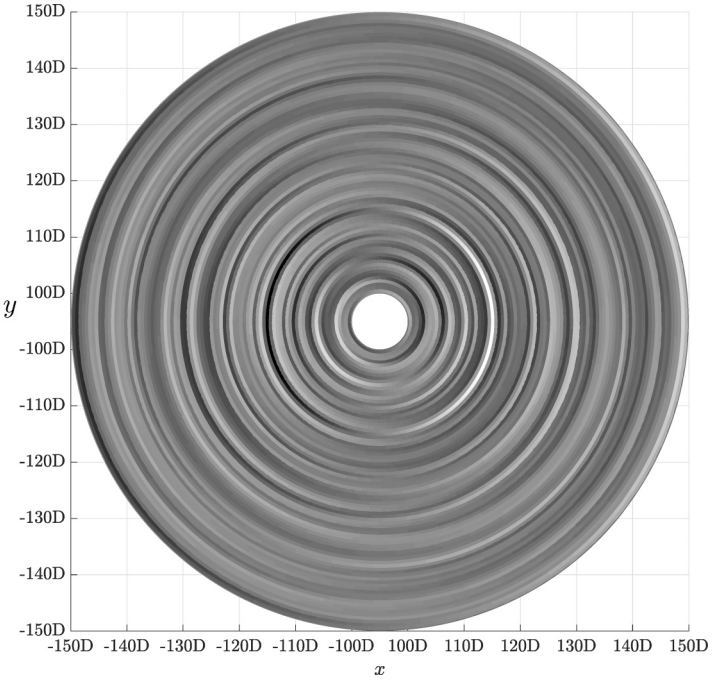

FIG. 7. The instantaneous total propeller sound field (p') at an arbitrary time step from $r = 100D$ to $150D$ in the xy plane. Note the axes in $(-100D, 100D)$ are not plotted to scale. The most intense oscillations occur in the positive and negative x directions, which agrees with the directivity in Fig. 4.

Figure 6 shows a comparison of the acoustic energy spectra from the PFD of the blades against (a) the PFD of the blades and hub, (b) CSA, and (c) FW-H. All spectra are calculated at an observer position of $\theta = 90^\circ$ to examine the effects of rotation and possible tonality of the sound; for observers out of the rotor plane the sound becomes intrinsically more broadband due to the nature of thrust generated sound. The signals are all broadband.

Figures 6(a) and 4 show that the hub itself is altering the sound intensity as well as the frequency content of this propeller. It appears that the hub affects sound at low and mid-frequencies, the higher frequencies appear to be the same in Fig. 4. Comparing with the PFD, both the CSA and FW-H have the largest differences occurring at high frequencies.

By comparing the spectra of FW-H and CSA, small differences can be seen at specific data points, but the overall shape is consistent. When the spectra are computed over an increased number of windows, the two signals converge.

Figure 7 shows the instantaneous sound field of the propeller from $r = 100D$ to $150D$ in the xy plane. Note that the axes on the interval $(-100D, 100D)$ are not plotted to scale to show the character of the sound. The largest amplitude oscillations are seen occurring in the positive and negative x directions which agrees qualitatively with Fig. 4. Last, the variety of wavelengths (frequencies) indicate the broadband nature of far-field radiated sound.

V. HUB SOUND

As was observed by Kumar and Mahesh [30], flow separation in the region near the hub and blade root creates a region of increased turbulence that persists for approximately three propeller diameters downstream. The elevated levels of unsteadiness on the hub surface contribute to the overall sound signature of the propeller. Figure 8 shows the RMS surface pressure on the propeller blades and hub, which indicates the strength of the acoustic source. Around the edge of the hub, where the flow

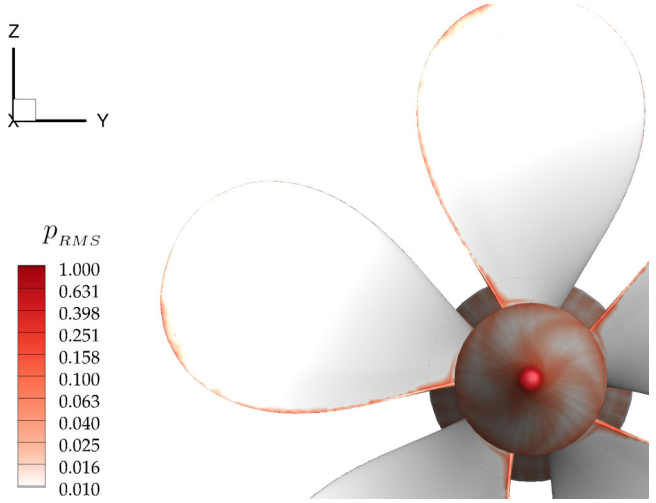

FIG. 8. Logarithmic contour levels of p_{RMS} on the propeller surface highlight the interaction between the blade roots and hub. The propeller rotates clockwise.

initially separates, there is a ring of high p_{RMS}; the flow separation is a significant source of hub sound.

The propeller wake consists of five helical tip vortices (one originating from each blade tip) and an axial hub vortex. LES captures the coherent vortical structures in the propeller wake as visualized using λ_2 criterion [58] colored with axial velocity, Fig. 9. The structures very near the propeller root are formed by the shedding of vorticity in the wakes of individual blades. The signatures of these root wakes can be seen very clearly on the surface of the hub and indicate interaction between the blade-root wakes and the hub.

Figure 10 shows the directivity of hub generated sound. The directivity is slightly elliptical, showing bias toward the rotor plane; the maximum SPL produced by the hub is 46.4 dB in the rotor plane and 44.3 dB along the axis of rotation. The spectrum of hub sound, $\theta = 90°$, is shown in Fig. 11. The overall shape of the spectrum is characteristic of turbulence. Compared with Fig. 6(a), the hub

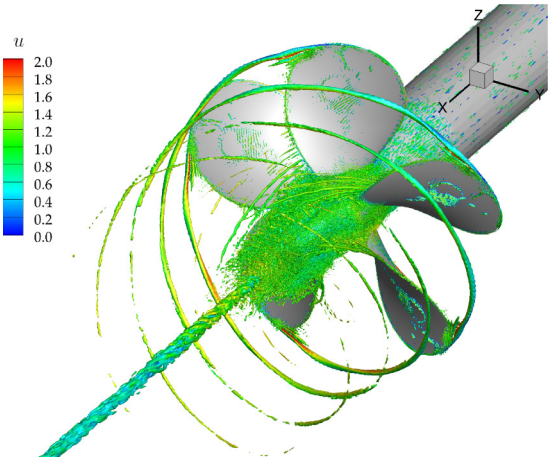

FIG. 9. Isocontour of λ_2 colored with axial velocity to show the hub, blade root, and tip vortices.

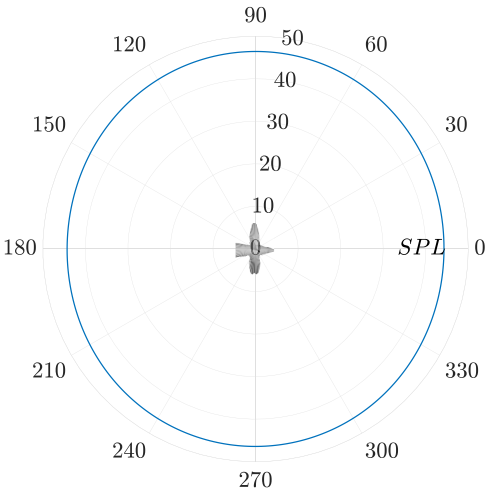

FIG. 10. Directivity of the hub's contribution to SPL, perpendicular to the rotor plane. The origin is 0 dB. The maximum value is 46.4 dB in the rotor plane and 44.3 dB along the rotation axis.

sound contains additional energy at many mid-to-low frequencies, likely due to the interaction of the individual blade-root wakes and the separated flow around the hub.

VI. BLADE SOUND

The circular directivity of Fig. 10 and the dipole shape of Fig. 4 reveal that the blades are the major source of sound for most observer locations. The discretization into a number of strips provides insight into the physics of blade loading and sound generation.

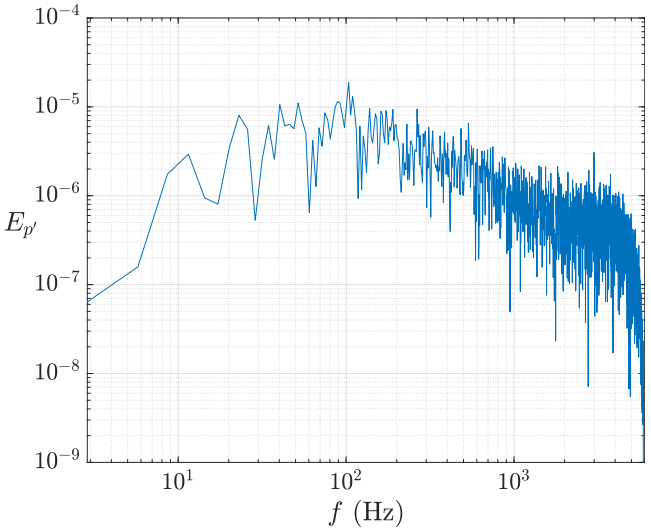

FIG. 11. Energy spectrum of the hub's contribution to overall sound calculated at an observer position of $\theta = 90^{\circ}$. The spectrum shows the broadband nature of the hub sound, which is characteristic of turbulence.

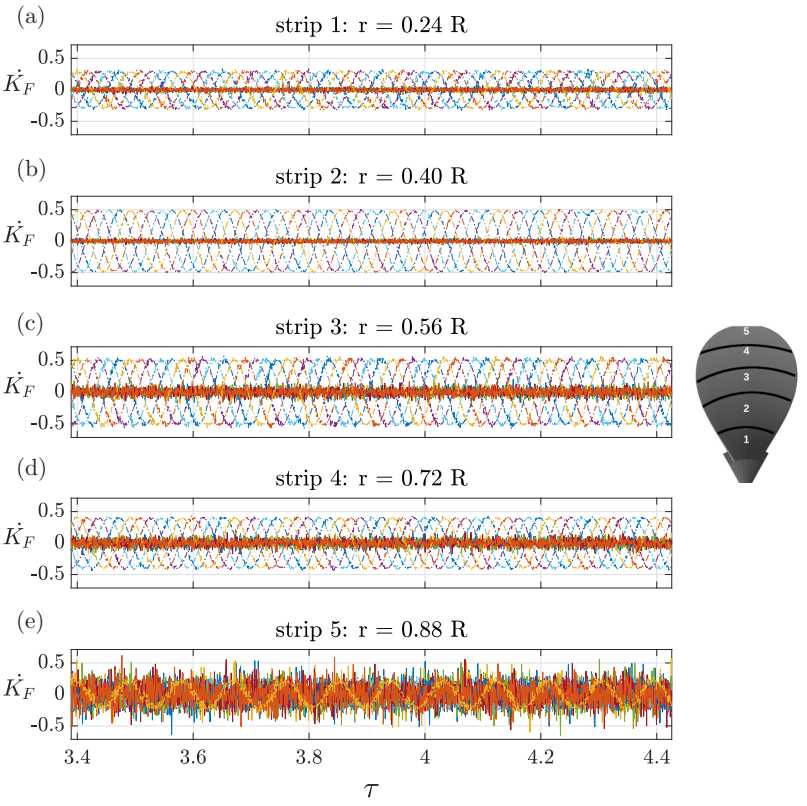

FIG. 12. Time histories of $\partial K_F/\partial\tau$ at five equally spaced radial location on the propeller, starting at (a) $r = 0.24R$ to (e) $r = 0.88R$. Time derivatives of the coefficients of thrust and the y component of the side force are plotted for all five blades at each radial location. Blade 1: $\dot{K}_T$ (——), $\dot{K}_{F_y}$ (— - —), blade 2: $\dot{K}_T$ (——), $\dot{K}_{F_y}$ (— - —), blade 3: $\dot{K}_T$ (——), $\dot{K}_{F_y}$ (— - —), blade 4: $\dot{K}_T$ (——), $\dot{K}_{F_y}$ (— - —), blade 5: $\dot{K}_T$ (——), $\dot{K}_{F_y}$ (— - —).

A. Blade loading

Figure 12 shows the time derivatives of both thrust and the y component of the side force for each of the five blades at five equally spaced radial locations. The z component is similar to the y component but is phase shifted due to the motion of the blades and is not shown.

It is clear that over most of the blade length, there are large side-force oscillations that dwarf the unsteadiness in thrust. The side-force variations are phase shifted by $1/5$ of a period between neighboring blades indicating that they are due to the motion of the blades under a quasisteady load. Note that when summed over all blades, an unsteady net side-force is recovered which fluctuates about the mean of zero.

Moving radially outward in Fig. 12, the amplitude peaks somewhere in the midspan and decreases toward the blade tip. This is contrasted by the marginal increase in thrust unsteadiness which jumps sharply near the blade tip, due to the unsteadiness of the tip vortex. The tip vortex is confined to a small region as seen in Fig. 9. In this region, the thrust unsteadiness is larger than that of the blade side force.

It should be pointed out that while the oscillations in side force are periodic and phase shift between blades, there are also small-amplitude, high-frequency oscillations that remain when the entire propeller is considered. The large-amplitude, low-frequency, periodic changes in side force (which produce tonal sound) destructively interfere resulting in small but nonzero rotor-plane sound observed in Fig. 4.

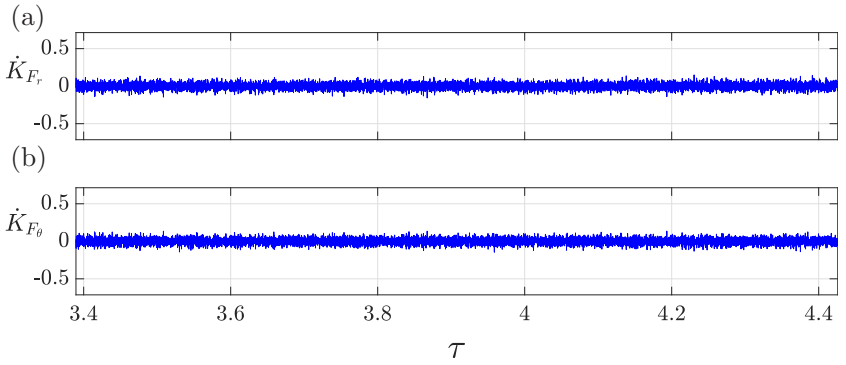

FIG. 13. Phase-averaged time histories of the nondimensional coefficients of blade radial force (a) and blade azimuthal force (b).

The propeller load can be decomposed into body-fitted radial and azimuthal components (rather than inertial y and z side-force components) and nondimensionalized in the same manner as K_T. Figure 13 shows that $\dot{K}_{F_r}$ and $\dot{K}_{F_\theta}$ oscillate about a constant load on each blade, implying that the the periodicity in Fig. 12 is due to the periodic motion of the blades and the decomposition into inertial forces, not a periodic flow phenomenon such as vortex shedding or ingestion of a velocity deficit. Furthermore, Fig. 14 shows the energy spectrum of the blade-frame azimuthal force at 10 locations along the blade. Note that near the blade root, energy is concentrated around low frequencies and the propeller rotation rate. The energy is distributed more evenly to the high frequencies moving radially outward, due to the increasing local chord based Reynolds number. This indicates that turbulent pressure fluctuations, and not periodic shedding of the vortex sheet, may be the primary source of noise on the blade.

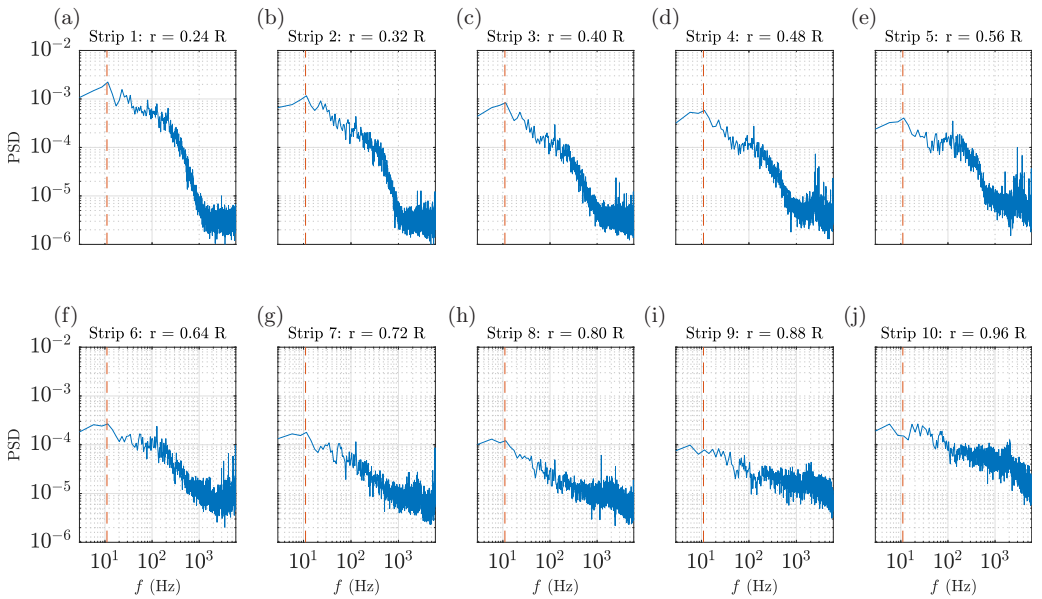

FIG. 14. Mean-blade spectra of azimuthal force on each of ten blade strip locations. The dashed vertical line represents the propeller rotation rate.

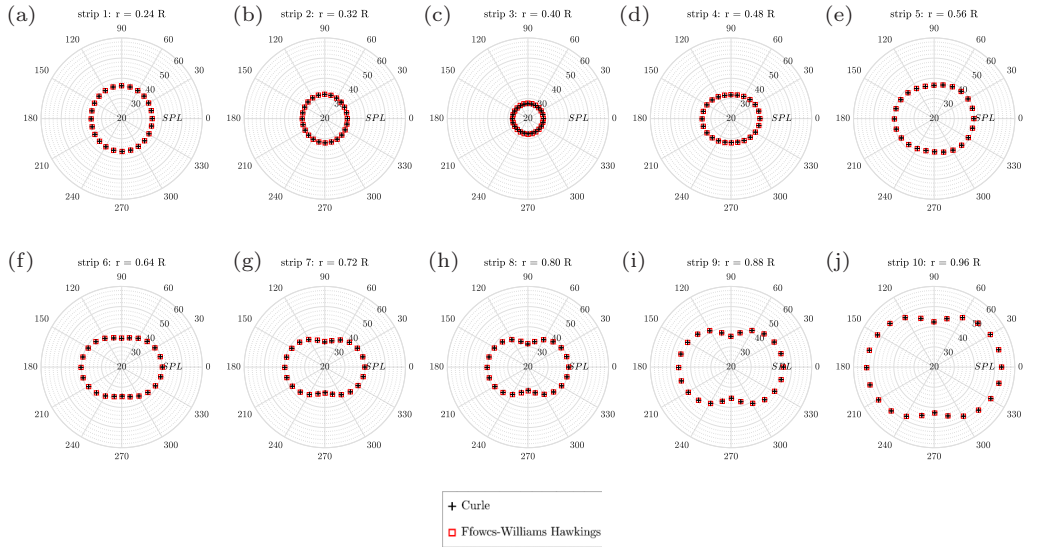

FIG. 15. Comparison of strip generated sound pressure level for the Curle strip analogy and Ffowcs-Williams and Hawkings strip analogy with ten strips per blade. The origin is set to 20 dB in all figures.

B. Blade strip sound

Figure 15 shows the directivity of each radial station, summed over all blades. It shows how the total sound levels change over the span of the blades. There are three clear regions, a blade root region (a–c), a blade loading region (d–h), and a tip vortex region (i, j). Figures 15(a)–15(c) all have the circular shape, mirroring the results seen in Sec. V. Similarly, the first strip is biased toward the rotor plane. This may indicate that interaction of the root wakes with the flow separation and hub vortex drives the unsteadiness on the surface of the blade root. The bias decays as the distance from the hub is increased as shown in Figs. 15(a)–15(d). Figures 15(d)–15(h) begin to take the shape of the propeller dipole; the lobes become more clearly defined approaching the area where the blade is maximally loaded ($\approx 0.72R$).

The last two subplots, Figs. 15(i) and 15(j), show that most of the blade sound is being produced at the tip. There is a small increase from strip eight [Fig. 15(h)] to strip nine [Fig. 15(i)], but there is a larger jump between strips nine [Fig. 15(i)] and ten [Fig. 15(j)]. The tip vortex is found to primarily affect the sound generated by thrust unsteadiness; an explanation for this is that the tip vortex is shed in the direction of the flow, seen in Figs. 12(d) and 12(e), where the amplitude of the thrust time derivative becomes much larger while the amplitude of the side-force time derivative remains unchanged. The large increase and localization of the sound indicates that the tip vortex (Fig. 9) dominates sound production over the rest of the blade.

Logarithmic contour levels of p_{RMS} in Fig. 16 highlight source regions located along the blade. The strongest sources are concentrated near the blade trailing edge. Moving radially along the trailing edge, starting at the root, it is evident that there are strong coherent regions connected by less coherent areas. There are three distinct regions, one near the hub, one along the mid-span, and one localized to the tip, following what was observed in Fig. 15. There is a streak in the chord-wise direction at the root that may indicate flow separation and interaction with the hub boundary layer. Figures 15 and 16 show that the tip zone is most important to capturing the level of total propeller sound.

The acoustic energy spectrum was calculated at each radial strip to investigate the sources. Figure 17 shows the mean energy spectrum of FW-H strip-generated sound, when the blades are considered independently; the peak at the propeller rotation frequency shows that the individual blades are creating strong, tonal sound. The method captures the first harmonic of the tones as well.

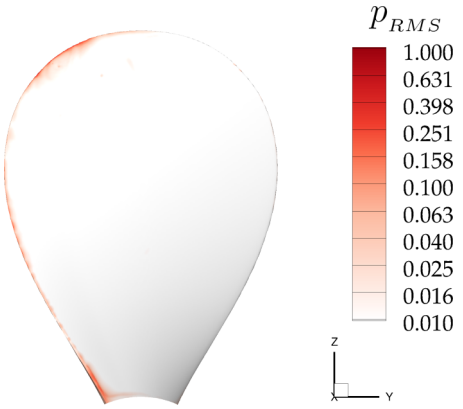

FIG. 16. Logarithmic contour levels of p_{RMS} on the propeller surface indicate the strength of the acoustic source. Propeller rotation is clockwise. The strongest sources are concentrated near the blade trailing edge.

Contrasting with Fig. 6, it is clear that these tones are absent when the entire propeller is considered. The cause of this behavior is the compactness of the problem at low frequencies; tones emanating from individual blades destructively interfere before reaching the far field. It appears that the tones are strongest halfway along where the blade is maximally loaded and has the largest chord-wise lifting surface. Figure 17 also shows a transfer of acoustic energy from midfrequencies, near the root, to high frequencies, at the tip. As the radius increases, the local Reynolds number increases and energy is transported to higher frequencies as the flow becomes more turbulent.

There are two main mechanisms by which turbulence could generate sound on the surface of the propeller. The first is by impingement of turbulence on the leading edge; the second mechanism is convection of boundary layer turbulence past the trailing edge. The singularity of the trailing edge leads to reorganization of the pressure field and improves the radiation efficiency of the otherwise inefficient turbulent-boundary-layer quadrupole source. Figure 18 is composed of three contour plots of turbulent kinetic energy (TKE) in the $x\theta$ plane at three locations along the blade, just above the

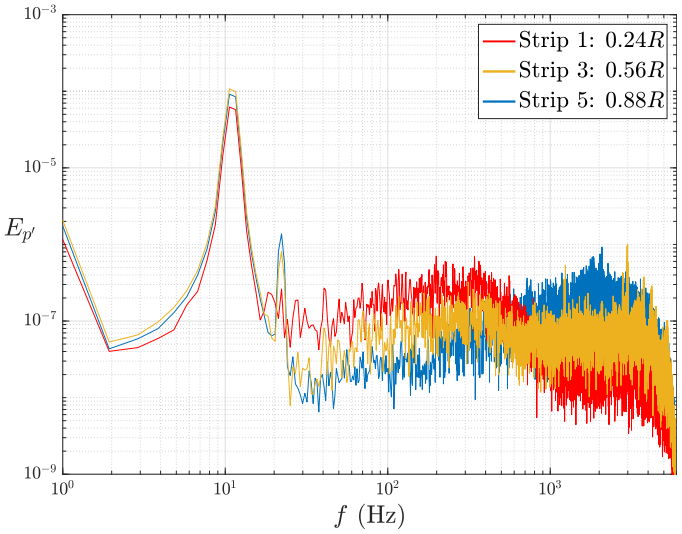

FIG. 17. Comparison of the mean energy spectra of strip generated sound from FW-H, with five strips per blade. Three strips are plotted to decrease clutter.

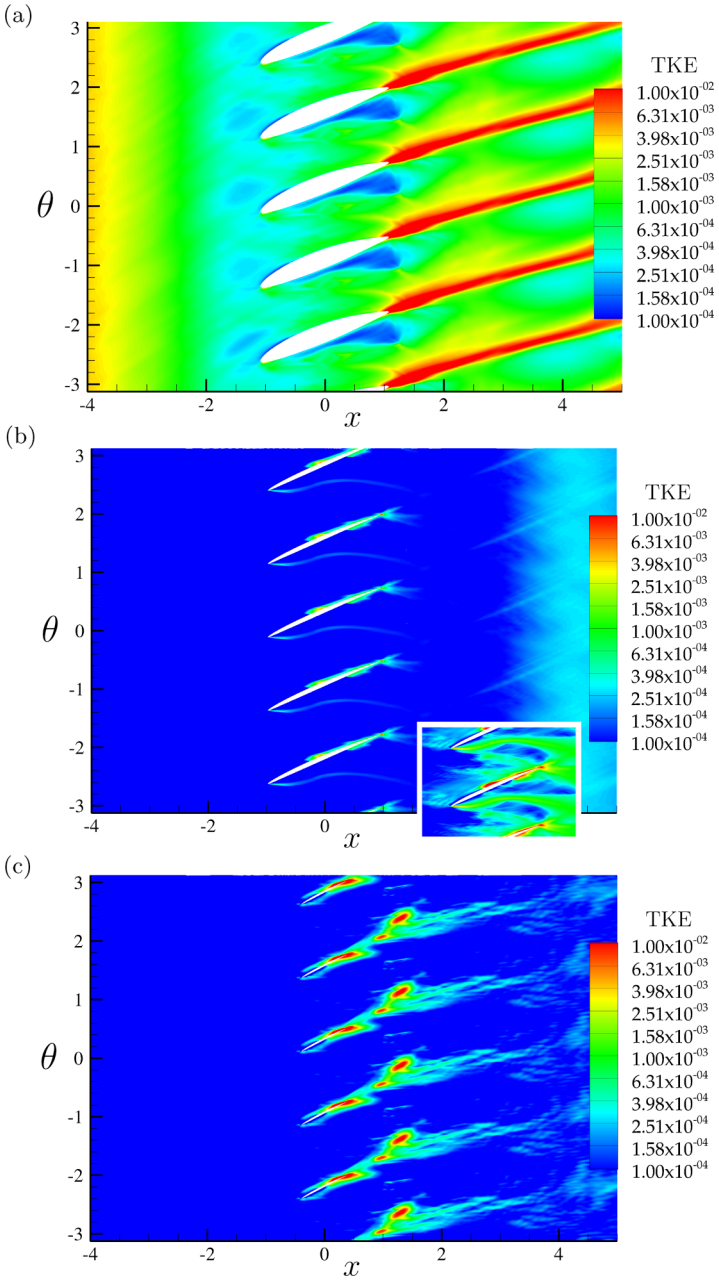

FIG. 18. Contour plots of turbulent kinetic energy (TKE) at three radial stations, just above the hub, $0.27R$ (a), near maximum blade loading, $0.72R$ (b), and near the blade tip, $0.96R$ (c). Note the contour levels of in the inset of (b) are decreased an order of magnitude.

hub, $0.27R$ [Fig. 18(a)], near location of maximum loading, $0.72R$ [Fig. 18(b)], and near the blade tip, $0.96R$ [Fig. 18(c)]. Note the contour levels of the inset of Fig. 18(b) are decreased an order of magnitude to highlight the trailing edge. These plots show that the main source of sound is turbulence, which is generated in the boundary layer and convected past the trailing edge. In all three plots, the largest amounts of TKE are located near the trailing edge.

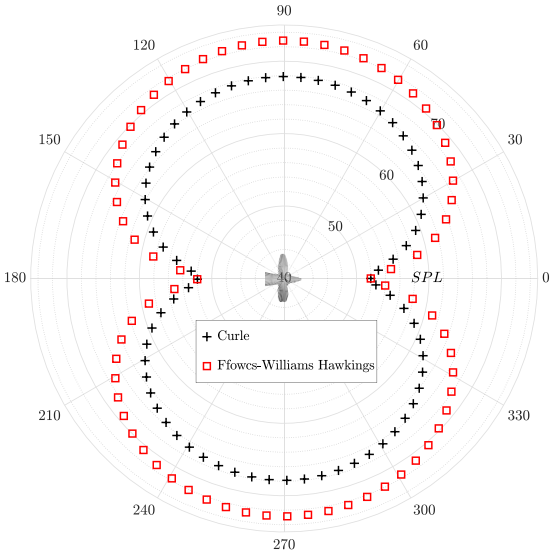

FIG. 19. Comparison of the blade generated sound pressure level from the Curle strip analogy and Ffowcs-Williams and Hawkings strip analogy. The origin is set to 40 dB to minimize empty plotting space.

Figure 18(a) shows that near the blade root, the flow upstream of the blades is turbulent. The flow is tripped by both the adverse pressure gradient created by the shaft contraction to the hub, as well as the change in velocity boundary conditions the flow experiences between the stationary shaft and the rotating hub. The flow separates at the trailing edge creating the turbulent root wakes.

Along the midspan [Fig. 18(b)], the blade is maximally loaded. There is turbulence generated on both the pressure and suction sides of the blade. At the trailing edge, there is still very concentrated but significant amount of turbulence present. The inset plot highlights the areas with the highest relative turbulence for the radius. There is a notable lack of turbulence at the leading edge.

At the blade tip [Fig. 18(c)], the flow is strongly unsteady due to the tip vortex. Again, there is a lack of turbulence at the leading edge, indicating that the primary mechanisms for blade generated sound are convection of boundary layer turbulence past the trailing edge in the presence of the unsteady tip vortex.

C. Total blade sound

Although in the far field the propeller directivity has a dipole shape parallel to the axis of rotation, Fig. 19 shows that the large-amplitude side-force oscillations over most of each blade (Fig. 12) behave like a much stronger dipole aligned with the rotor plane. The individual blade produces a large amount of sound in the rotor plane as seen in Fig. 19; the blade sound (Fig. 20) is strongly tonal. The propeller is acoustically compact at the energetic tones which leads to destructive interference in the far field. Presumably, the major axis of the directivity Fig. 4 would shift as the observer approaches the near field.

Figure 20 shows a comparison of the blade spectrum for both the CSA and FW-H methods. The additional thickness and force-acceleration terms of the FW-H lead to prediction of stronger tones in the rotor plane.

VII. MODELING IMPLICATIONS

Important inputs to the noise models based on the work of Amiet [6] are spectra of surface pressure and the spanwise correlation length. The spectral properties of surface pressure have been discussed

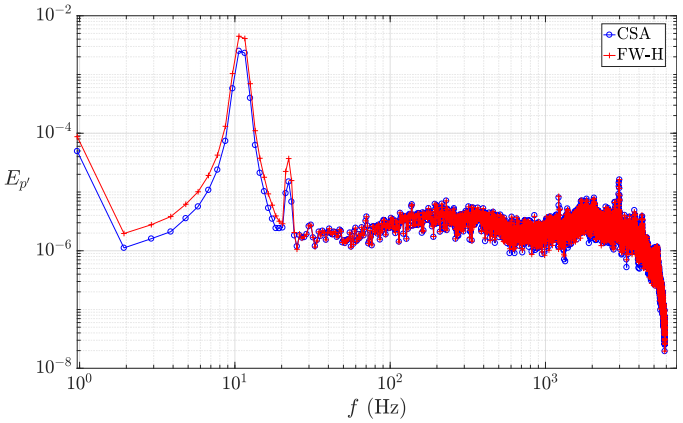

FIG. 20. Comparison of the energy spectra of blade generated sound between the Curle strip analogy and Ffowcs-Williams and Hawkings strip analogy.

via propeller loading. For the current operating conditions, unsteadiness due to the shedding of the tip vortex is found to be the primary source of sound. Furthermore, along the blade, self noise is generated by convection of boundary layer turbulence past the blade trailing edge. This is compounded at the blade tip, where the unsteady tip vortex is shed, producing the majority of the total sound. The sound is found to be broadband overall. Locally on the blade, energy is transferred from midfrequencies to high frequencies with the radially increasing local Reynolds number.

Palumbo [59] notes that the source correlation length ($\mathcal{L}$) and coherence length (ℓ) are related, but not equivalent. Coherence length is a function of both frequency, position, and separation and is band specific whereas correlation length (a function of space and separation) is a wide-band, time-domain variable, which is more convenient for describing the broadband nature of the propeller sources. The sources are decomposed into the time derivatives of thrust ($\dot{T}$) and the blade-frame azimuthal ($\dot{F}_\theta$) and radial ($\dot{F}_r$) forces to examine source correlation without bias due to the rotational motion. Correlation length is computed as the maximum cross-correlation (χ) over all lags ($\mathbb{T}$) between radial locations r_1 and r_2, normalized by the auto-correlations and integrated over the blade length at each location,

$$\mathcal{L}(r_1) = \int_0^L \frac{|\max_{\mathbb{T}}(\chi(r_1,r_2,\mathbb{T}))|^2}{\chi(r_1,r_1,0)\chi(r_2,r_2,0)} dr_2. \tag{12}$$

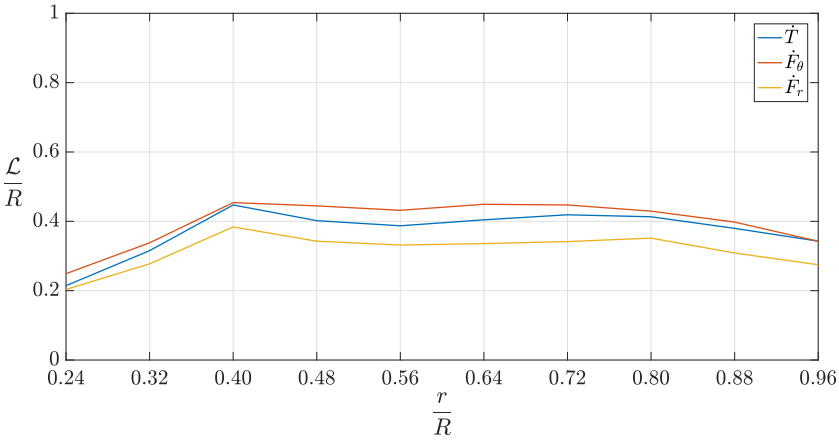

FIG. 21. The radial variation of the source correlation length, $\mathcal{L}$.

Note that the cross-correlation is a function of both r_1 and r_2. No assumptions have been made regarding the homogeneity of the flow or of the sources radially along the blade.

Figure 21 shows the radial variation of $\mathcal{L}$ normalized by blade length; unity implies that the sources are correlated over the length of the blade. For all three sources, the mean-radial values of $\mathcal{L}$ are less than $0.4R$. The regions where the blade is most turbulent ($\frac{r}{R} \leqslant 0.4$ and $\frac{r}{R} \geqslant 0.88$) are correlated over shorter distances, as expected. Note that for both propeller-strip discretizations, the characteristic size of the strip (Δr) is less than the minimum correlation length on the blade.

VIII. SUMMARY

Sound is predicted for flow over a propeller at design operating condition. The accuracy of the sound prediction depends on the accuracy of the flow field, hence LES is used to compute far-field noise. Each blade of the propeller is decomposed into multiple radial strips and the sound at an observer radius of 100 diameters is computed using three different acoustic analogies: PFD, CSA, and FW-H strip acoustic analogy. Far-field sound is computed for five and ten strips per blade for both the CSA and FW-H.

The generated sound is dependent on the unsteadiness of the propeller loading. For the present operating condition, it is seen that the propeller hub and locations near the blade tips are where the most unsteadiness occurs while the blade is maximally loaded in the midspan, near $0.7R$. The effect of the tip vortex is found to be highly localized to the outermost strip, which is confirmed by the flow field. The propeller is found to produce maximum levels of sound along the axis of rotation, which decay to a minimum in the rotor plane for the far field.

The propeller hub is found to be a quasiomnidirectional sound generator, most important to overall sound levels in the rotor plane. The primary mechanism of sound generation is suggested to be flow separation on the hub as well as interaction of the surface with the turbulent wakes of the blade roots. The generated sound is broadband and contains significant energy at midlow frequencies.

The individual blades produce strongly tonal low frequency sound at the rotation rate. At this frequency, the propeller is acoustically compact and the sound destructively interferes in the far field. At high frequency, the propeller and individual blades are broadband; in this broadband region, there is a shift of energy from the mid-frequencies to high frequencies, moving radially outward, due to the increasingly turbulent nature of the flow. The blades are found to generate a significant level of self noise; the mechanism of sound generation is found to be convection of turbulence in the boundary layer past the blade trailing edge. Additionally, unsteadiness confined to the tip vortex region couples with turbulent self noise to generate the majority of the propeller sound.

Results from the three applied methods agree very well. The propeller becomes acoustically noncompact for sound at frequencies above 1 000 Hz leading to over prediction of sound levels by the PFD. The turbulent nature of the propeller sound results in frequencies above 1 000 Hz containing significant acoustic energy. Consistent results are found for a discretization of as few as five and ten strips per blade. In the far field, the thin nature the blades and slow rotation of the propeller result in negligible difference between the CSA and more computationally expensive FW-H.

ACKNOWLEDGMENTS

This work is supported by the United States Office of Naval Research (ONR) under ONR Grants N0014-14-1-0289 and N0014-14-1-0304 with Dr. Ki-Han Kim as technical monitor. The computations were made possible through the computing resources provided by the US Army Engineer Research and Development Center (ERDC) in Vicksburg, Mississippi on the Cray XE6, Copper and Garnet, of the High Performance Computing Modernization Program (HPCMP). The authors also acknowledge the Minnesota Supercomputing Institute at the University of Minnesota for providing resources that contributed to the research reported in this paper.

[1] W. K. Blake, *Mechanics of Flow-Induced Sound and Vibration. Volume I: General Concepts and Elementary Sources* (Academic Press, San Diego, 1986).
[2] J. Carlton, *Marine propellers and propulsion* (Butterworth-Heinemann, London, 2011).
[3] L. Gutin, Uber das schallfeld einer rotierenden luftschraube, Phys. Z. Sowjetunion **9**, 57 (1936) [On the sound field of a rotating propeller, N.A.C.A. TM. No. 1195 (1948)].
[4] M. J. Lighthill, On sound generated aerodynamically. I. General theory, in *Proceedings of the Royal Society of London A: Mathematical, Physical and Engineering Sciences*, Vol. 211 (The Royal Society, London, 1952), pp. 564–587.
[5] J. E. Ffowcs-Williams and D. L. Hawkings, Sound generation by turbulence and surfaces in arbitrary motion, Philos. Trans. R. Soc. London **264**, 321 (1969).
[6] R. K. Amiet, Acoustic radiation from an airfoil in a turbulent stream, J. Sound Vib. **41**, 407 (1975).
[7] J. E. Ffowcs-Williams and L. H. Hall, Aerodynamic sound generation by turbulent flow in the vicinity of a scattering half plane, J. Fluid Mech. **40**, 657 (1970).
[8] M. S. Howe, A review of the theory of trailing edge noise, J. Sound Vib. **61**, 437 (1978).
[9] M. V. Lowson and J. B. Ollerhead, A theoretical study of helicopter rotor noise, J. Sound Vib. **9**, 197 (1969).
[10] G. P. Succi, Design of Quiet Efficient Propellers, SAE Technical Paper 790584 (1979), https://doi.org/10.4271/790584.
[11] F. Farassat and G. P. Succi, A review of propeller discrete frequency noise prediction technology with emphasis on two current methods for time domain calculations, J. Sound Vib. **71**, 399 (1980).
[12] W. R. Graham, A comparison of models for the wavenumber-frequency spectrum of turbulent boundary layer pressures, J. Sound Vib. **206**, 541 (1997).
[13] M. Roger, Broadband noise from lifting surfaces analytical modeling and experimental validation, in *Noise Sources in Turbulent Shear Flows: Fundamentals and Applications* (Springer, Vienna, 2013), pp. 289–344.
[14] V. P. Blandeau and P. F. Joseph, Validity of Amiet's model for propeller trailing-edge noise, AIAA J. **49**, 1057 (2011).
[15] M. Roger and S. Moreau, Back-scattering correction and further extensions of Amiet's trailing-edge noise model. Part I: Theory, J. Sound Vib. **286**, 477 (2005).
[16] S. Moreau and M. Roger, Back-scattering correction and further extensions of Amiet's trailing-edge noise model. Part II: Application, J. Sound Vib. **323**, 397 (2009).
[17] M. Roger and A. Carazo, Blade-geometry considerations in analytical gust-airfoil interaction noise models, in *Proceedings of the 16th AIAA/CEAS Aeroacoustics Conference, Stockholm, Sweden* (AIAA, Reston, VA, 2010), p. 3799.
[18] S. A. L. Glegg, E. Kawashima, F. Lachowski, W. Devenport, and N. Alexander, Inflow distortion noise in a non axisymmetric flow, in *Proceedings of 19th AIAA/CEAS Aeroacoustics Conference, Berlin* (AIAA, Reston, VA 2013), pp. 27–29.
[19] M. A. Morton, W. Devenport, W. N. Alexander, S. A. L. Glegg, and A. Borgoltz, Rotor Inflow Noise Caused by a Boundary Layer: Inflow Measurements and Noise Predictions, Ph.D. thesis, University Libraries, Virginia Polytechnic Institute and State University (2012).
[20] S. A. L. Glegg, M. Morton, and W. Devenport, Rotor inflow noise caused by a boundary layer: theory and examples, in *Proceedings of the 18th AIAA/CEAS Aeroacoustics Conference* (AIAA, Reston, VA, 2012).
[21] E. Envia, Fan noise source diagnostic test-vane unsteady pressure results, in *Proceedings of the 8th AIAA/CEAS Aeroacoustics Conference, Breckenridge, CO* (AIAA, Reston, VA, 2002) p. 2430.
[22] H. Posson, S. Moreau, and M. Roger, Fan-OGV broadband noise prediction using a cascade response, in *Proceedings of the 15th AIAA/CEAS Aeroacoustical Conference, Miami, FL* (AIAA, Reston, VA, 2009), p. 3150.
[23] M. Roger and S. Moreau, Broadband self-noise from loaded fan blades, AIAA J. **42**, 536 (2004).
[24] K. S. Brentner and F. Farassat, Modeling aerodynamically generated sound of helicopter rotors, Prog. Aeronaut. Sci. **39**, 83 (2003).
[25] A. Tadamasa and M. Zangeneh, Numerical prediction of wind turbine noise, Renew. Energy **36**, 1902 (2011).

[26] C. Arakawa, O. Fleig, M. Iida, and M. Shimooka, Numerical approach for noise reduction of wind turbine blade tip with earth simulator, J. Earth Simulat. **2**, 11 (2005).
[27] J. Wang, K. Wang, and M. Wang, Computation of rotor noise generation in grid turbulence using large-eddy simulation, in *Proceedings of the 21st AIAA/CEAS Aeroacoustics Conference* (AIAA, Reston, VA, 2015), p. 2982.
[28] J. Wang, K. Wang, and M. Wang, Computation of the noise of rotor interaction with a turbulent wake, in *Proceedings of the 22nd AIAA/CEAS Aeroacoustics Conference* (AIAA, Reston, VA, 2016), p. 2998.
[29] J. Wang, K. Wang, and M. Wang, Large-eddy simulation study of rotor noise generation in a turbulent wake, in *Proceedings of the 23rd AIAA/CEAS Aeroacoustics Conference, Denver, CO* (AIAA, Reston, VA, 2017).
[30] P. Kumar and K. Mahesh, Large eddy simulation of propeller wake instabilities, J. Fluid Mech. **814**, 361 (2017).
[31] J. Keller, P. Kumar, and K. Mahesh, Large eddy simulation of propeller in forward mode of operation, in *Proceedings of the 5th International Symposium on Marine Propulsors, Espoo, Finland* (2017).
[32] A. Segalini and P. Inghels, Confinement effects in wind-turbine and propeller measurements, J. Fluid Mech. **756**, 110 (2014).
[33] K. Mahesh, P. Kumar, A. Gnanaskandan, and Z. Nitzkorski, LES applied to ship research, J. Ship Res. **59**, 238 (2015).
[34] M. Germano, U. Piomelli, P. Moin, and W. H. Cabot, A dynamic subgrid-scale eddy viscosity model, Phys. Fluids A **3:7**, 1760 (1991).
[35] D. K. Lilly, A proposed modification of the Germano subgrid-scale closure model, Phys. Fluids A **4:3**, 633 (1992).
[36] A. Verma and K. Mahesh, A lagrangian subgrid-scale model with dynamic estimation of lagrangian time scale for large eddy simulation of complex flows, Phys. Fluids **24**, 085101 (2012).
[37] N. Park and K. Mahesh, Reduction of the Germano-identity error in the dynamic Smagorinsky model, Phys. Fluids (1994–present) **21**, 065106 (2009).
[38] K. Mahesh, G. Constantinescu, and P. Moin, A numerical method for large-eddy simulation in complex geometries, J. Comput. Phys. **197**, 215 (2004).
[39] M. Vyšohlid and K. Mahesh, Large eddy simulation of crashback in marine propellers, in *Proceedings of the 26th Symposium on Naval Hydrodynamics, Rome, Italy* (2006).
[40] P. Chang, M. Ebert, Y. L. Young, Z. Liu, K. Mahesh, H. Jang, and M. Shearer, Propeller forces and structural responses to crashback, in *Proceedings of the 27th Symposium on Naval Hydrodynamics, Seoul, Korea* (2008).
[41] H. Jang and K. Mahesh, Large eddy simulation of ducted propulsors in crashback, in *Proceedings of the 27th Symposium on Naval Hydrodynamics* (2008).
[42] H. Jang and K. Mahesh, Large eddy simulation of crashback in ducted propulsors with stator blades, in *Proceedings of the 29th Symposium on Naval Hydrodynamics* (2012).
[43] H. Jang and K. Mahesh, Large eddy simulation of flow around a reverse rotating propeller, J. Fluid Mech. **729**, 151 (2013).
[44] A. Verma, H. Jang, and K. Mahesh, The effect of an upstream hull on a propeller in reverse rotation, J. Fluid Mech. **704**, 61 (2012).
[45] P. Kumar and K. Mahesh, Analysis of marine propulsor in crashback using large eddy simulation, in *Proceedings of the 4th International Symposium on Marine Propulsors, Austin, TX* (2015).
[46] P. Kumar and K. Mahesh, Toward large eddy simulation of hull-attached propeller in crashback, in *Proceedings of the 31st Symposium on Naval Hydrodynamics, Monterey, CA* (2016).
[47] D. H. Bridges, A detailed study of the flowfield of a submarine propeller during a crashback maneuver, Tech. Rep. MSSU-ASE-04-1 (Department of Aerospace Engineering, Mississippi State University, 2004).
[48] M. E. Goldstein, *Aeroacoustics* (McGraw-Hill, New York, 1976).
[49] M. S. Howe, *Theory of Vortex Sound* (Cambridge University Press, Cambridge, 2003), p. 232.
[50] S. A. L. Glegg and W. Devenport, *Aeroacoustics of Low Mach Number Flows: Fundamentals, Analysis, and Measurement* (Academic Press, San Diego, 2017).

[51] N. Curle, The influence of solid boundaries upon aerodynamic sound, Proc. R. Soc. London **231**, 505 (1955).
[52] W. K. Blake, *Mechanics of Flow-Induced Sound and Vibration. Volume II: Complex Flow-Structure Interactions* (Academic Press, San Diego, 1986).
[53] M. V. Lowson and J. B. Ollerhead, Studies of helicopter noise, US Army Aviation Materiel Laboratories Technical Report TR, 68–60 (1969).
[54] M. V. Lowson, The sound field for singularities in motion, in *Proceedings of the Royal Society of London A: Mathematical, Physical and Engineering Sciences*, Vol. 286 (The Royal Society, London, 1965), pp. 559–572.
[55] R. Hecker and K. Remmers, Four quadrant open-water performance of propellers 3710, 4024, 4086, 4381, 4382, 4383, 4384, and 4426, David Taylor Naval Ship Research and Development Center, report NSRADC, 417–H01 (1971).
[56] S. Jessup, C. Chesnakas, D. Fry, M. Donnelly, S. Black, and J. Park, Propeller performance at extreme off design conditions, in *Proceedings of the 25th Symposium on Naval Hydrodynamics, St. John's, Canada* (2004).
[57] S. Jessup, D. Fry, and M. Donnelly, Unsteady propeller performance in crashback conditions with and without a duct, in *Proceedings of the 26th Symposium on Naval Hydrodynamics, Rome, Italy* (2006).
[58] J. Jeong and F. Hussain, On the identification of a vortex, J. Fluid Mech. **285**, 69 (1995).
[59] D. Palumbo, Determining correlation and coherence lengths in turbulent boundary layer flight data, J. Sound Vib. **331**, 3721 (2012).